Eightfold quantum Hall phases in a time reversal symmetry broken tight binding model

Sudarshan Saha,[1,2,*] Tanay Nag,[3,†] and Saptarshi Mandal[1,2,‡]

[1]*Institute of Physics, Bhubaneswar- 751005, Odhisa, India*

[2]*Homi Bhabha National Institute, Mumbai - 400 094, Maharashtra, India*

[3]*Institute für Theorie der Statistischen Physik, RWTH Aachen University, 52056 Aachen, Germany*

(Received 24 February 2021; revised 9 June 2021; accepted 15 June 2021; published 24 June 2021)

We consider a time reversal symmetry (TRS) broken Kane-Mele model superimposed with a Haldane model and chart out the phase diagram using spin Chern number to investigate the fate of the quantum anomalous Hall insulator (QAHI) and quantum spin Hall insulator (QSHI) phases. Interestingly, in addition to the QSHI and QAHI phase, the phase diagram unveils a quantum anomalous spin Hall insulator (QASHI) phase where only one spin sector is topological. We also find multicritical points where three or four topological phase boundaries coalesce. These topological phases are protected by an effective TRS and a composite antiunitary particle-hole symmetry leading to remarkable properties of edge modes. We find spin-selective, spin-polarized, and spin-neutral edge transport in the QASHI, QSHI, and QAHI phases, respectively. Our study indicates that the robustness of the topological phase mainly depends on the spin gap which does not necessarily vanish at the Dirac points across a topological phase transition. We believe that our proposals can be tested in the near future using recent experimental advancements in solid state and cold atomic systems.

DOI: 10.1103/PhysRevB.103.235154

Recently various noninteracting quantum Hall systems such as the quantum anomalous Hall insulator (QAHI) [1,2] and quantum spin Hall insulator (QSHI) [3–5] and many more [6–9] have been investigated in various topological context. The QAHI and QSHI are best characterized by the quantized charge and spin current, respectively. This is intimately connected with the fact that QAHI [1] breaks time reversal symmetry (TRS) while QSHI does not [3]. The spin-orbit coupling serves as a basic ingredient for the QSH effect to occur. It has been shown that the bulk topological invariant Chern number [10] (spin Chern number [11]) can successfully predict the number of edge states (spin polarized channels) in QAHI (QSHI) phases [12,13]. Another widely used topological invariant namely, Z_2 index can equivalently classify TR invariant system [3,14–18]. Thereafter it becomes an important question that what would be the fate of the QSHI phase in the absence of TRS.

In order to search for the answers, TRS breaking terms such as exchange field [19,20], magnetic doping [21,22], and staggered magnetic flux [23] are introduced in the QSH system to obtain a QAH effect. Remarkably, even though Z_2 index fails to characterize the topological nature of the phase, the spin Chern number persists to be a relevant topological invariant distinguishing a TRS broken QSHI phase from a QAHI phase. The QSH [3] and QAH [1] models have been generalized to various theoretical platforms [24,25] and realized in experiments [26,27]. All these studies motivate us to consider a Kane-Mele model infused with a Haldane model such that the TRS is broken by staggered magnetic flux associated with next nearest neighbor (NNN) hopping and an intrinsic spin-orbit coupling (SOC) term. To be precise, we ask the following questions: (1). How do the Haldane and Kane-Mele phase diagrams modify? (2). Are there any new topological phases apart from QSHI and QAHI phases? (3). Can the spin Chern number successfully describe all the phases?

To this end, we first demonstrate how the Haldane (Kane-Mele) phases evolve with the Rashba and SOC terms (NNN hopping and magnetic flux) [see Figs. 1, 2, and 3]. The zeros of bulk energy gap determine the topological phase boundaries and the finite spin gap [20,28] provides the robustness of the spin Chern number $(C_\uparrow, C_\downarrow)$ [14,29] of a topological phase. The QASHI [QSHI] phases are denoted by $(C_\uparrow, 0)$ and $(0, C_\downarrow)$ [$(C_\uparrow, C_\downarrow)$ with $C_\uparrow \neq C_\downarrow \neq 0$] while QAHI phase is designated by $C_\uparrow = C_\downarrow \neq 0$. In confirmation of bulk-boundary correspondence, we find spin-selective, -polarized, and -neutral transport in QASHI, QSHI, and QAHI phases in the band structure in semi-infinite geometry with zig-zag edge (see Fig. 4). These findings are further explained by the low energy version of the model where evolution of spin dependent Haldane gap with various parameters are demonstrated. These topological phases are protected under emerging antiunitary symmetries that couple with the chirality of the flux. In essence, considering a simple flux induced TRS broken QSHI model, our study uncovers many extraordinary features in a systematic manner and also opens up the possibility of practical device applications in the future.

The Hamiltonian we consider here is given as

$$H = -t_1 \sum_{\langle ij \rangle} c_i^\dagger c_j + iV_R \sum_{\langle ij \rangle} c_i^\dagger (\vec{\sigma} \times \vec{d}_{ij})_z c_j + M \sum_i c_i^\dagger \sigma_z c_i + t_2 \sum_{\langle\langle ij \rangle\rangle} e^{i\phi_{ij}} c_i^\dagger c_j + \frac{iV_{so}}{\sqrt{3}} \sum_{\langle\langle ij \rangle\rangle} e^{i\phi_{ij}} \nu_{ij} c_i^\dagger \sigma^z c_j, \quad (1)$$

*sudarshan@iopb.res.in

†tnag@physik.rwth-aachen.de

‡saptarshi@iopb.res.in

where c_i represents the fermion spinor $(c_{i\uparrow}, c_{i\downarrow})$; $V_{\rm so}$ and V_R represent the SOC and Rashba interaction strength, respectively. The model incorporates a spin-independent NN (NNN) hopping denoted by t_1 (t_2). The phase factor $e^{i\phi_{ij}}$ comes due to the staggered magnetic flux as described in the Haldane model [1]. The factor $\nu_{ij} = (\mathbf{d}^1_{ij} \times \mathbf{d}^2_{ij})_z$ and the lattice vectors are same as mentioned in Kane-Mele model [4]. The important point to note here is that the SOC term acts as the spin dependent NNN hopping of strength $V_{\rm so}$ where spin-dependent magnetic fluxes are essentially coupled to the electron momenta. M represents the inversion breaking mass term.

Before proceeding further, we emphasize the key features of the model Hamiltonian as given in Eq. (1) and their physical implications in detail. We know that in the limit $V_R = V_{\rm so} = 0$, the model contains two copies of the Haldane model. In this case the spin indices are irrelevant. The topological phases follow the condition $M < |3\sqrt{3}t_2 \sin\phi|$ [1]. The TRS is broken there and both the spin sectors have the same spin Chern number. To understand the phases, obtained in the Kane-Mele model, we note that they correspond to $\phi = 0, t_2 = 0$, but do contain the next nearest neighbor spin dependent hopping with complex magnitudes. The fact that the complex NNN spin dependent hopping changes sign under spin flipping implies the restoration of the TRS. The spin Chern numbers of opposite spin sectors are opposite. The total spin Chern number must add up to zero owing to the TRS invariant nature of the system. As long as TRS is preserved an additional interaction such as the Rashba spin-orbit interaction is not able to change the scenario and new phases will not appear. Interestingly when the TRS is broken by introducing a flux in the same spirit of the Haldane model, one expects new topological phases to appear. In particular, we introduce the magnetic flux in the SOC term so that the spin dependent NNN hopping acquires complex amplitudes. The sum of spin Chern number over all the spin sectors is no longer constrained to be zero. This observation opens up the possibility of QASHI phase where one spin sector is topological and the other is not.

We now discuss in detail the phase diagram obtained by investigating the Hamiltonian (1) in momentum space. One can obtain the momentum space Hamiltonian after Fourier transformation of Eq. (1) as given by

$$H(\boldsymbol{k}) = \sum_{i=0}^{9} n_i(\boldsymbol{k})\, \Gamma_i \tag{2}$$

with $\Gamma_i = \sigma_i \otimes \tau_0$ for $i = 1, 2, 3$, $\Gamma_{i+3} = \sigma_i \otimes \tau_1$ for $i = 1, 2$, $\Gamma_{i+5} = \sigma_i \otimes \tau_2$ for $i = 1, 2$, $\Gamma_8 = \sigma_3 \otimes \tau_3$, $\Gamma_9 = \sigma_0 \otimes \tau_3$ and $\Gamma_0 = \sigma_0 \otimes \tau_0$. Here $\boldsymbol{\sigma}$ and $\boldsymbol{\tau}$ represent orbital and spin degrees of freedom while writing the Hamiltonian in the basis $(c_{A\uparrow}, c_{A\downarrow}, c_{B\uparrow}, c_{B\downarrow})$. The components n_i are given by $n_0 = 2t_2 f(\boldsymbol{k}) \cos\phi$, $n_1 = -t_1(1 + 2h(\boldsymbol{k}))$, $n_2 = -2t_1 \sin\frac{\sqrt{3}k_y}{2} \cos\frac{k_x}{2}$, $n_3 = M - 2t_2\, g(\boldsymbol{k}) \sin\phi$, $n_4 = \frac{V_R}{\sqrt{3}} \sin\frac{\sqrt{3}k_y}{2} \cos\frac{k_x}{2}$, $n_5 = \frac{V_R}{\sqrt{3}}(h(\boldsymbol{k}) - 1)$, $n_6 = -V_R \cos\frac{\sqrt{3}k_y}{2} \sin\frac{k_x}{2}$, $n_7 = V_R \sin\frac{\sqrt{3}k_y}{2} \sin\frac{k_x}{2}$, $n_8 = \frac{V_{\rm so}}{3} g(\boldsymbol{k}) \cos\phi$, $n_9 = \frac{V_{\rm so}}{3} f(\boldsymbol{k}) \sin\phi$, with $f(\boldsymbol{k}) = 2\cos\frac{\sqrt{3}k_y}{2} \cos\frac{k_x}{2} + \cos k_x$, $g(\boldsymbol{k}) = 2\cos\frac{\sqrt{3}k_y}{2} \sin\frac{k_x}{2} - \sin k_x$, $h(\boldsymbol{k}) = \cos\frac{\sqrt{3}k_y}{2} \cos\frac{k_x}{2}$. We note that for $V_R = V_{\rm so} = 0$, the model (1) reduces to two copies of the Haldane model [that breaks TRS, $\mathcal{T}H(\boldsymbol{k})\mathcal{T}^{-1} \neq H(-\boldsymbol{k})$ with $\mathcal{T} = (I \otimes \tau_2)i\mathcal{K}$, $\mathcal{K}$ being the complex conjugation] with spin up and down block. On the other hand, for $t_2 = \phi = 0$, it reduces to Kane-Mele model (that preserves TRS).

To understand the physical connection of the TRS breaking in the presence of intrinsic spin-orbit coupling, we investigate the following terms deeply: $H_{A\uparrow A\uparrow}(\boldsymbol{k}) = n_0 + n_3 + n_8 + n_9 = (f(\boldsymbol{k})\frac{V_{\rm so}}{3} - 2g(\boldsymbol{k})t_2)\sin\phi + (g(\boldsymbol{k})\frac{V_{\rm so}}{3} - 2f(\boldsymbol{k})t_2)\cos\phi + M$ and $H_{A\downarrow A\downarrow}(\boldsymbol{k}) = n_0 + n_3 - n_8 - n_9 = -(f(\boldsymbol{k})\frac{V_{\rm so}}{3} + 2g(\boldsymbol{k})t_2)\sin\phi - (g(\boldsymbol{k})\frac{V_{\rm so}}{3} + 2f(\boldsymbol{k})t_2)\cos\phi + M$. We notice that in the absence of $V_{\rm so}$, $H_{A\uparrow A\uparrow}(\boldsymbol{k}) = H_{A\downarrow A\downarrow}(\boldsymbol{k})$. The similar line of argument is also applicable for $H_{B\uparrow B\uparrow}(\boldsymbol{k})$ and $H_{B\downarrow B\downarrow}(\boldsymbol{k})$. In the semiclassical picture this refers to a situation when the spin degrees of freedom are suppressed and only the orbital / charge degrees of freedom remain active just as the case for the Haldane model. The band inversion conditions, estimated at Dirac points, takes the same form irrespective of their spin components. However when the spin-orbit interaction is considered, we observe that it affects the different spin components in the opposite way. This can be thought of as a $\boldsymbol{k}$-dependent Zeeman field splitting between spin up and down components. Thus we see a competition in energy scale due to orbital degrees of freedom and spin degrees of freedom. As a result, the band inversion condition of both the spin component at the two Dirac points are no longer interdependent. In the rest of the paper, we consider $t_1 = 1.0$ and $t_2 = 0.5$ without loss of generality.

Now it may be pertinent to digress a little and discuss the topological characterization of various phases. We may note that to describe a two-dimensional electronic system involving explicit spin degrees of freedom, two topological invariants, namelythe Z_2 invariant [4] and spin Chern number [11] were proposed in close succession. In the present case with TRS breaking magnetic flux, the spin Chern number continues to work while the Z_2 invariant ceases [14]. We hence use the spin Chern number $C_\uparrow$ and $C_\downarrow$ to classify different phases of the Hamiltonian as given in Eq. (2). In order to numerically compute the spin Chern number, one has to construct the projector $P(\boldsymbol{k}) = |V_1(\boldsymbol{k})\rangle\langle V_1(\boldsymbol{k})| + |V_2(\boldsymbol{k})\rangle\langle V_2(\boldsymbol{k})|$ with $|V_1(\boldsymbol{k})\rangle$ and $|V_2(\boldsymbol{k})\rangle$ being the eigenvectors corresponding to two valence bands with energies $E_1(\boldsymbol{k})$, $E_2(\boldsymbol{k}) < 0$. Now by diagonalizing the four-dimensional projected spin operator $\tilde{S}(\boldsymbol{k}) = P(\boldsymbol{k})(\sigma_0 \otimes \tau_3)P(\boldsymbol{k})$, we can obtain four eigenvectors $|\psi_{1,2,3,4}(\boldsymbol{k})\rangle$ corresponding to four eigenvalues $\epsilon_{1,2,3,4}(\boldsymbol{k})$ with $|\epsilon_1(\boldsymbol{k})| = \epsilon_4(\boldsymbol{k}) \neq 0$, $|\epsilon_2(\boldsymbol{k})| = \epsilon_3(\boldsymbol{k}) \simeq 0$ (within numerical accuracy) and $\epsilon_1(\boldsymbol{k}) < \epsilon_4(\boldsymbol{k})$. We further use the four-component eigenvectors $|\psi_1(\boldsymbol{k})\rangle$ and $|\psi_4(\boldsymbol{k})\rangle$, corresponding to two nonzero eigenvalues, to numerically compute $C_\uparrow$ and $C_\downarrow$, respectively. Here we follow the Fukui's method in the $\boldsymbol{k}$-space to compute them [16]. Instead of constructing a four-dimensional projected spin operator $\tilde{S}(\boldsymbol{k})$, using the property of projector operator $P(\boldsymbol{k})$, a two-dimensional effective projected spin operator $\mathcal{S}_{ij}(\boldsymbol{k}) = \langle V_i(\boldsymbol{k})|\sigma_0 \otimes \tau_3|V_j(\boldsymbol{k})\rangle$ with $i, j = 1, 2$, can be alternatively used to compute the spin Chern numbers [20,29].

To begin with, we show the phase diagram in $M - \phi$ plane by keeping $V_{\rm so} = 1.0$ fixed as shown in Fig. 1(a) and 1(b) for $V_R = 0$ and 0.5, respectively. As the modification over Haldane's phase diagram, we find that a finite $V_{\rm so}$ in

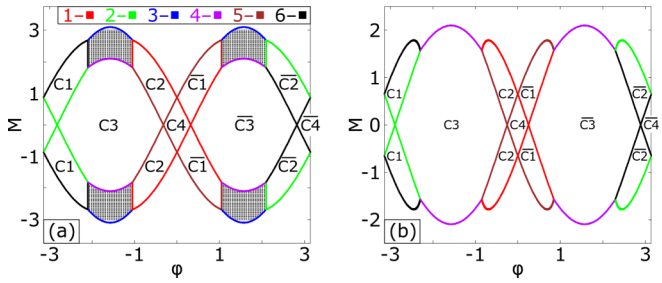

FIG. 1. Here we show the effect of V_R for a fixed $V_{so} = 1.0$ in M-ϕ phase diagram. (a) and (b) are plotted with $V_R = 0.0$ and $V_R = 0.5$ respectively. The indices within a given phase refer the values of $(C_\uparrow, C_\downarrow)$: $C1 = (0, 1)$, $C2 = (1, 0)$, $C3 = (1, 1)$, $C4 = (1, -1)$ and $\overline{Cn} = -Cn$ with $n = 1, 2, 3, 4$. The phase boundary is obtained by the zeros of band gap [30] and the color codes refer to the relevant band gap equations. The spin gap vanishes in critical phase as denoted by the assembly of black dots in (a).

Hamiltonian (1) results in two additional topological phases namely, QSHI $[(C_\uparrow, C_\downarrow)$ with $C_\uparrow = -C_\downarrow = \pm 1]$ and QASHI $[(C_\uparrow = 0, C_\downarrow = \pm 1)$ or $(C_\uparrow = \pm 1, C_\downarrow = 0)]$ phases. The size of QAHI phases, characterized by spin Chern number $(C_\uparrow, C_\downarrow)$ with $C_\uparrow = C_\downarrow = \pm 1$, gets reduced as compared to QAHI phases in the Haldane model; $(1, 1)$ and $(-1, -1)$ phases are, respectively, encapsulated by QASHI phases $(0, 1)$, $(1, 0)$ and $(0, -1)$, $(-1, 0)$ from below and above. While the two adjacent QAHI phases are connected by QSHI phases $(1, -1)$ and $(-1, 1)$. The color coded phase boundaries are assigned to the zeros of the respective energy gap equations [30]. It is noteworthy that $\phi \to -\phi$, implies $C_\uparrow \to -C_\downarrow$ and $C_\downarrow \to -C_\uparrow$ for the QASHI and QAHI phases. This correspondence holds also for QSHI phase that maps to itself. The underlying reason could be the helical edge modes are a time reversed partner of each other in the QSHI phase.

Strikingly, we encounter an extended critical phase, denoted by an assembly of black dots, within which the spin gap vanishes identically as shown in Fig. 1(a) [28]. This caplike critical phase cannot be characterized by the spin Chern number. The vertical height (horizontal width) of the critical phase decreases (increases) with increasing V_R (such that $V_R \leqslant V_{so}$) while the size of QASHI phases reduces without qualitatively deforming their phase boundaries. The QASHI phases vanish and the critical phase extends between $-\pi < \phi < \pi$ when $V_R > V_{so}$ as depicted in Figs. 2(a) and 2(b). In other words, the critical phases are bounded by violet phase boundaries from outside for $V_R > V_{so}$. This phase becomes the widest when $V_{so} = 0$ [see Fig. 2(a)]. Upon introduction of V_{so}, the size of QAHI phases reduces as well as the critical phase becomes narrower [see Fig. 2(b)]. Finally, when $V_{so} \geqslant V_R$, QASHI phases start to appear near $\phi = 0$ and $\pm\pi$. The violet phase boundaries expand with increasing V_R and it fully extends $-\pi < \phi < \pi$ when $V_R \geqslant V_{so}$. The gapless critical phase, otherwise bounded from outside, will now be bounded from inside by the violet phase boundaries as soon as V_{so} exceeds V_R. The exact relation between V_{so} and V_R can be found from the gap equation corresponding to the violet phase boundary [30].

We now investigate the phase diagram in the V_R-M plane to elucidate the modification over Kane-Mele phases namely,

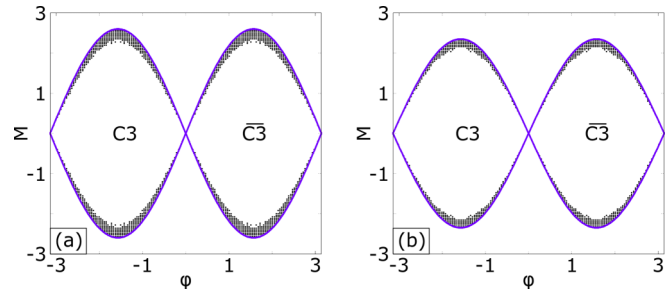

FIG. 2. Here we investigate the effect of V_{so} for a fixed $V_R = 1.0$ in M-ϕ phase diagram. (a) and (b) are plotted for $V_{so} = 0.0$ and $V_{so} = 0.5$, respectively. The definition of Cn and $\overline{Cn}$ are provided in the caption of Fig. 1. The spin gap vanishes in the critical phase, denoted by the assembly of black dots, that gets narrower with increasing V_{so}.

QSHI phases as shown in Figs. 3(a) and 3(b) for $\phi = 0$ and $-\pi/4$, respectively. The distinctive feature is that finite ϕ is able to break the QSHI phase $(1, -1)$ into QASHI phase $(1, 0)$ and QAHI phase $(1, 1)$, while NNN hopping t_2 alone does not affect the existing phase diagram. Notably, the QAHI phase originates between the two lobes of the QASHI phase. We note that TRS breaking uniform exchange field can lead to QAHI phases [20]. The staggered magnetic flux ϕ associated with NNN hopping t_2 and spin dependent hopping V_{so} acts as a key ingredient to generate all the above phases simultaneously. It is to be noted that QASHI phases appear when $V_R < V_{so}$. The color coded phase boundaries indicates that the identical QASHI phases for positive and negative M are bounded by same gap equations.

Below, we emphasize a few essential conclusions from these phase diagrams. The QAHI (QSHI) lobes of the Haldane (Kane-Mele) model dismantle into a variety of phases in the presence of V_R and V_{so} (t_2 and ϕ) giving rise to multicritical points where multiple topological phase boundaries coalesce. Across a phase boundary, separating two topological phases, $|\Delta C_\uparrow + \Delta C_\downarrow|$ can only become unity where $\Delta C_\uparrow$ ($\Delta C_\downarrow$) measures the difference in $C_\uparrow$ ($C_\downarrow$) among the two adjacent topological phases separated by a phase boundary. This situation no longer holds generically when we encounter a multicritical point. The most important finding of our work is the emergence of a QASHI phase where only one spin component is topologically protected leaving the other to be trivially gapped out. Even though, this type of phase has been found in magnetically doped QSHI material [19,21,22], ours is a tight binding model hosting these phases naturally.

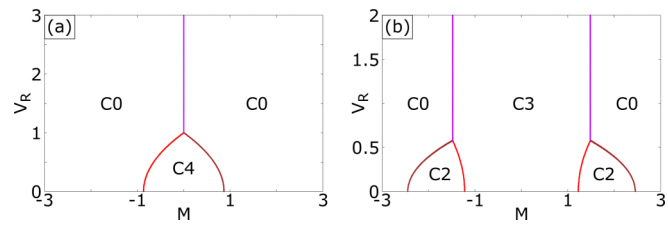

FIG. 3. We here demonstrate that how a QSHI phase gives rise to QAHI and QASHI phase by varying ϕ in M- V_R plane keeping $V_{so} = 1.0$ fixed. (a) and (b)correspond to $\phi = 0.0$ and $\phi = -\pi/4$, respectively. The definition of Cn and $\overline{Cn}$ are provided in the caption of Fig. 1.

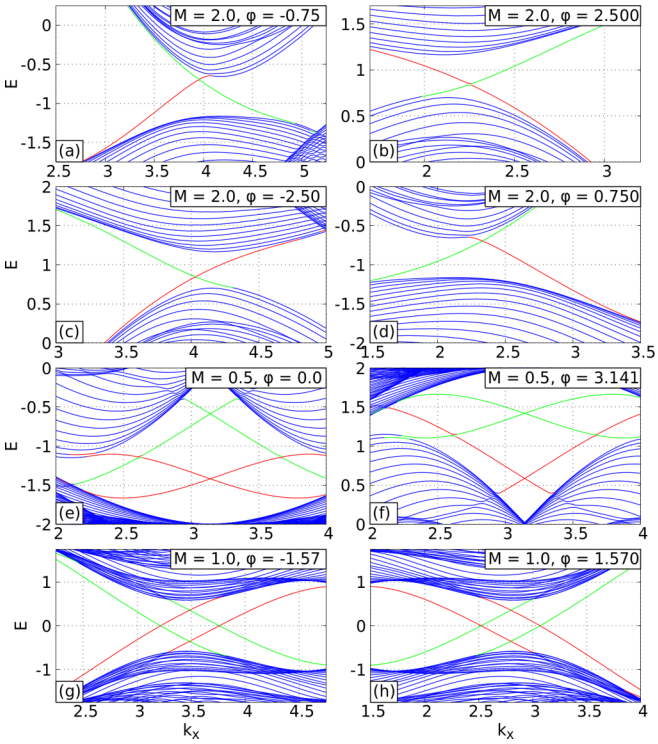

FIG. 4. Here we display the edge modes for various topological phases: QASHI phase in (a), (b), (c), (d) for $(1, 0)$, $(-1, 0)$, $(0, 1)$ and $(0, -1)$, respectively; QSHI phases in (e) and (f) for $(1, -1)$ and $(-1, 1)$, respectively; QAHI phases in (g) and (h) for $(1, 1)$ and $(-1, -1)$, respectively. The red line (green) refers to the localization of edge modes at top (bottom) part of the semi-infinite zig-zag chain.

We now describe the edge state in the zig-zag edge ribbon geometry (periodic in x direction and finite in y direction) and its connection to the bulk invariant as a probe to understand the bulk-boundary correspondence [31]. In Figs. 4(a), 4(b), 4(c), and 4(d), we depict the edge modes for $(1, 0)$, $(-1, 0)$, $(0, 1)$ and $(0, -1)$, respectively. To this end we generalize the bulk-boundary correspondence for QAHI and QSHI [1,4] to QASHI: $C_\sigma = N^\sigma_{\rm RM} - N^\sigma_{\rm LM}$, where $N^\sigma_{\rm RM}$ ($N^\sigma_{\rm LM}$) represents the number of right (left) moving edge modes for spin $\sigma = \uparrow, \downarrow$. We note that edge modes are not completely spin polarized as far as their numerical calculations are concerned. We assign an edge state to be spin up (down) if it is maximally populated by spin up (down) states. Turning to the helical edge states in the QSHI phase, as shown in Figs. 4(e) and 4(f), the spin dependent chiral motion is clearly captured where up (down) spin traverses in a clockwise (anticlockwise) manner along the edges of the system. This results in two types of QSHI phases with spin Chern number $(1, -1)$ and $(-1, 1)$ depending on the chirality of the spin-polarized edge state. Finally, we show the chiral edge states of $(1, 1)$ and $(-1, -1)$ QAHI phases, respectively, in Figs. 4(g) and 4(h). In this case, both the spin up and down edge states share same chirality while traversing along the boundaries of the system. Therefore, using the bulk-boundary correspondence, we can successfully explain that the spin dependent edge states in different phases are related by the spin Chern number of the underlying phases.

Another very intriguing fact that we notice is except for $\phi = \pm\pi/2$, where the QAHI phases host zero energy chiral edge states as shown in Figs. 4(g) and 4(h), all the other values of $\phi \neq \pm\pi/2$ support finite energy edge states if there exists a topological phase. The edge modes do not show any avoided level crossing structures that are observed for QSHI in presence of magnetically doping and exchange field [20–22]. Therefore, staggered flux induced topological phases are intrinsically different from the above cases even though the TRS is broken in both the situations. An effective TRS emerges implying $E(\pi - k, \phi) = E(\pi + k, -\phi)$ in our case. Even more surprisingly, edge modes are further protected by a composite antiunitary symmetry ensuring $E(\pi - k, \pi - \phi) = -E(\pi + k, \pi + \phi)$. Thus the twin effect of these antiunitary symmetries allows one the mapping $C_\uparrow \to -C_\downarrow$ and $C_\downarrow \to -C_\uparrow$ under $\phi \to -\phi$. This further guarantees the existence of zero energy chiral edge modes for any topological phase obtained at $\phi = \pm\pi/2$.

Having extensively explored the lattice model, we now resort to the low energy model for better understanding behind the emergence of different phases. Expanding around the Dirac points $\alpha = \pm 1$, we obtain $n_1 = -\alpha\sqrt{3}t_1 k_x/2$, $n_2 = \sqrt{3}t_1 k_y/2$, $n_3 = M + \alpha 3\sqrt{3}t_2 \sin\phi\theta(\mathbf{k})$, $n_4 = -V_R k_y/4$, $n_5 = -V_R/\sqrt{3} + \alpha V_R k_x/4$, $n_6 = \alpha V_R/\sqrt{3} + V_R k_x/4$, $n_7 = -\alpha 3V_R k_y/4$, $n_8 = -\alpha(\sqrt{3}/2)V_{\rm so}\cos\phi\theta(\mathbf{k})$, $n_9 = -(V_{\rm so}/2)\sin\phi\theta(\mathbf{k})$ with $\theta(\mathbf{k}) = (1 - |k|^2/4)$. At the Dirac points, the eigenenergies take the following form: $E_{1,4} = (w_1 + w_4 \pm \lambda_1^{14})/2$, $E_{2,3} = (w_2 + w_3 \pm \lambda_2^{23})/2$ with $w_1 = n_3 + n_8 + n_9$, $w_2 = n_3 - n_8 - n_9$, $w_3 = -n_3 - n_8 + n_9$, $w_4 = -n_3 + n_8 - n_9$, $r_1 = -n_5 - n_6$ and $r_2 = n_6 - n_5$, $\lambda_i^{jk} = \sqrt{4r_i^2 + (w_j - w_k)^2}$. Let us now start with a simple case $V_R = 0$ leading to the energy gap for spin up $\Delta E^\uparrow_{AB} = w_1 - w_3$, and spin down $\Delta E^\downarrow_{AB} = w_2 - w_4$. In this case, the low energy model closely follows the Bernevig-Hughes-Zhang model for a HgTe quantum well [32] enabling us investigate different phases in a similar spirit. A topological phase is ensured by opposite signs of the gap at two Dirac points $\boldsymbol{k}_1$ and $\boldsymbol{k}_2$: $\Delta E^{\uparrow(\downarrow)}_{AB}(\boldsymbol{k}_1)\Delta E^{\uparrow(\downarrow)}_{AB}(\boldsymbol{k}_2) < 0$. The different combination of the above product can, in principle, determine various topological phases.

For the QASHI phases with $(C_\uparrow, 0)$ $[(0, C_\downarrow)]$, one can find that the spin up [down] sector is only topologically gapped out leaving the other spin sector to be trivial. For the QSHI phase with $(C_\uparrow = \pm 1, C_\downarrow = \mp 1)$, one can find different combinations of topological gap in both the spin sectors. In the case of QAHI phase with $(C_\uparrow = \pm 1, C_\downarrow = \pm 1)$, the same combination of topological gap occurs in both the spin sectors. Denoting $x_{\zeta,\xi} = M + \zeta 3\sqrt{3}t_2 \sin\phi + \xi(V_{\rm so}/2)\sin\phi$, we find that for the topological spin up channel with $C_\uparrow \neq 0$, $x_{+-}x_{-+} < 0$; on the other hand, for the topological spin down channel with $C_\downarrow \neq 0$, $x_{++}x_{--} < 0$. The phase boundaries across which $C_\uparrow$ ($C_\downarrow$) changes are obtained by solving for M from $x_{\pm\mp}$ ($x_{\pm\pm}$)=0. This further explains the observation that $C_\uparrow$ and $C_\downarrow$ can only jump by unity across a phase boundary separating two different topological phases. However, there exist multicritical points in the phase diagram where more than two phases converge including nontopological phases. At these points, the spin Chern number can jump by more than unity. Without Rasbha interaction $V_R = 0$, one can

observe QAHI, QSHI, and QASHI phases in various parameter regimes as shown in Figs. 1 and 3, can be explained by the above low energy analysis.

Now, we extend our analysis for finite $V_R \neq 0$ using the low energy formulation. We note that phase boundaries are modified without altering the topological nature of the phases in the presence of V_R provided $V_{so} \neq 0$ and $\phi \neq 0$. This suggests that phases, present in the absence of V_R, are adiabatically connected while Rashba interaction is turned on. The principle for a phase being topological remains unaltered, however, their explicit forms are modified. Denoting $y_\eta = \eta\sqrt{3}(V_{so}/2)\cos\phi$ and $z_{\zeta,\xi} = \sqrt{4V_R^2/3 + x_{\zeta,\xi}^2}$, we find $\Delta E_{AB}^{\uparrow\downarrow}(\boldsymbol{k}_1) = \pm y_- + |x_{+,-}|\mathrm{sgn}(x_{+,-}) + z_{+,+}$, $\Delta E_{AB}^{\uparrow\downarrow}(\boldsymbol{k}_2) = \pm y_+ + |x_{-,+}|\mathrm{sgn}(x_{-,+}) + z_{-,-}$. For spin up (down) sector to be topological, the following condition needs to be satisfied $[y_- + |x_{+,-}|\mathrm{sgn}(x_{+,-}) + z_{+,+}][y_+ + |x_{-,+}|\mathrm{sgn}(x_{-,+}) + z_{-,-}] < 0$ $([y_+ + |x_{+,-}|\mathrm{sgn}(x_{+,-}) + z_{+,+}][y_- + |x_{-,+}|\mathrm{sgn}(x_{-,+}) + z_{-,-}] < 0)$. In order to obtain physical phase boundaries $z_{\zeta,\xi}^2$ has to be positive, which yields the modification of phase boundaries in presence of V_R [30]. It is important to note that in addition to the $V_R = 0$ case, the relative strength between $V_{so}\sin\phi$ and $\sqrt{3}V_R/2$ terms also play an important role in determining the phase boundaries. For example, the phase boundary is substantially modified with a new topological phase once ϕ becomes nonzero (i.e., TRS is broken) as shown in Figs. 3(a) and 3(b). Relying on the structure of topological gap at Dirac points, one can define the spin Chern number in an effective manner as follows:

$$C_\sigma = \tfrac{1}{2}\big[\mathrm{sgn}\big(\Delta E_{AB}^{\sigma}(\boldsymbol{k}_2)\big) - \mathrm{sgn}\big(\Delta E_{AB}^{\sigma}(\boldsymbol{k}_1)\big)\big], \tag{3}$$

with $\sigma = \uparrow, \downarrow$. Now we elaborate the role of the spin gap defined as $\Delta\mathcal{E}_A^{\uparrow\downarrow} = E_A^{\uparrow} - E_A^{\downarrow}$, and $\Delta\mathcal{E}_B^{\uparrow\downarrow} = E_B^{\uparrow} - E_B^{\downarrow}$ at two Dirac points in examining the underlying stability for topological transitions. It is indeed necessary to have finite spin gap $\Delta\mathcal{E}_A^{\uparrow\downarrow}, \Delta\mathcal{E}_B^{\uparrow\downarrow} \neq 0$, in order to characterize a phase with $(C_\uparrow, C_\downarrow)$ [28]. Therefore, the robustness and stability of the topological invariant is determined by the finiteness of the spin gap. Interestingly, our numerical calculation with lattice model suggests that spin gap can vanish at any arbitrary point inside the momentum Brillouin zone for $\phi \neq 0$. This is in contrast to the energy gap, obtained from the lattice model, that only vanishes at Dirac points.

In conclusion, we consider the TRS broken Kane-Mele model merged with the Haldane model where intrinsic SOC is coupled with staggered magnetic flux to investigate the fate of QSHI phases. We remarkably find new topological phases namely, the QASHI phase and extended critical region in addition to the QAHI and QSHI phase while studying the spin Chern number $(C_\uparrow, C_\downarrow)$. The QASHI phase, characterized by $(0, C_\downarrow)$ and $(C_\uparrow, 0)$, supports spin-selective transport where one spin channel is topologically gapped out leaving the other component trivially gapped. The other two topological phases namely, QSHI and QAHI phases exhibit spin-polarized and spin-neutral edge transport in accordance with spin Chern number. In short, superimposing the Haldane model with the Kane-Mele model, we can successfully unify all possible types of QH phases for two-dimensional noninteracting system in a single phase diagram. The topological phases in this model are preserved by an effective TRS and a composite particle-hole symmetry. We show that the findings from the lattice model can be understood from a low energy model around the Dirac point. We also provide an effective description of spin Chern number, based on the low energy model, that corroborates with the lattice calculation. Surprisingly, the band gap turns out to be decisive in the topological characterization while stability and robustness is determined by the finiteness of the spin gap. In terms of the future applications, our study can become useful in exploring the spin entanglement in different phase [33,34] and disorder induced Anderson QSHI phases [35].

Before ending we shall discuss the connection of work to recent experimental advancements. We note that in optical lattice platform SOC is theoretically proposed [36–40] and experimentally realized [41–44]. In particular, the method of producing complex next-nearest neighbor hopping, which was employed earlier to realize the Haldane model, can be utilized further to the case of spin dependent hopping with complex amplitudes [26]. The suggested procedure involves the application of spin-dependent force that is caused by an oscillating magnetic field gradient. By adjusting the oscillating field and the mirror position together, the complex phase factor, appearing for the opposite spin component, may be engineered. As far as the real materials are concerned there have been several proposals and experimental realizations of the QAH effect which include the magnetic-ion-doped HgTe quantum well [21], topological insulator surfaces [45], transition metal oxides [46,47], and engineered graphene [19,48]. The Haldane-like complex next nearest hopping amplitude was found in a series of Fe-based honeycomb ferromagnetic insulators, $A\mathrm{Fe}(\mathrm{PO}_4)_2 (A = \mathrm{Ba}, \mathrm{Cs}, \mathrm{K}, \mathrm{La})$ which possess Chern bands [49]. The spin dependent hopping can be engineered in the materials such as, $A\mathrm{Fe}(\mathrm{PO}_4)_2$, graphene with magnetic impurity [19,50], magnetically ordered two-dimensional materials [51,52], transition metal oxide heterostructures [46], Skyrmion lattice [53–56] and magnetic insulators MnTe, MnSe that could then serve as the potential candidates to realize our model in principle. On the other hand, the materials with intrinsic spin-orbit coupling that host the QAH effect [24,57] may be promising candidates if the spin-orbit interaction is controlled by using the methods outlined before. Moreover the external pressure could be a useful way to control the Rashba spin interaction [58] whereas the intrinsic spin orbit interaction can be manipulated by suitable doping and other interactions [59–61]. Though the quantitative prescription of such schemes is beyond the scope of present study and will be presented elsewhere, we expect that with the state of the art experiments in the near future such a controlled spin-dependent hopping can be realized. Apart from the possible experimental realizations, our work has a significant amount of technological relevance in the context of spintronics within modern electronics, spin field effect transistors, and magnetic field sensors of hard disk drives [62–64].

S.S. thanks SAMKHYA: High Performance Computing Facility provided by the Institute of Physics, Bhubaneswar. T.N. thanks B. Roy for useful discussions. S.M. thanks A.K. Nandy for useful discussions.

[1] F. D. M. Haldane, Phys. Rev. Lett. **61**, 2015 (1988).

[2] M. Onoda and N. Nagaosa, Phys. Rev. Lett. **90**, 206601 (2003).

[3] C. L. Kane and E. J. Mele, Phys. Rev. Lett. **95**, 226801 (2005).

[4] C. L. Kane and E. J. Mele, Phys. Rev. Lett. **95**, 146802 (2005).

[5] B. A. Bernevig and S. C. Zhang, Phys. Rev. Lett. **96**, 106802 (2006).

[6] K. von Klitzing, Rev. Mod. Phys. **58**, 519 (1986).

[7] J. Maciejko, T. L. Hughes, and S.-C. Zhang, Annu. Rev. Condens. Matter Phys. **2**, 31 (2011).

[8] M. Z. Hasan and C. L. Kane, Rev. Mod. Phys. **82**, 3045 (2010).

[9] C.-X. Liu, S.-C. Zhang, and X.-L. Qi, Annu. Rev. Condens. Matter Phys. **7**, 301 (2016).

[10] Q. Niu, D. J. Thouless, and Y. S. Wu, Phys. Rev. B **31**, 3372 (1985); M. Kohmoto, Ann. Phys. **160**, 343 (1985).

[11] D. N. Sheng, Z. Y. Weng, L. Sheng, and F. D. M. Haldane, Phys. Rev. Lett. **97**, 036808 (2006); L. Sheng, D. N. Sheng, C. S. Ting, and F. D. M. Haldane, *ibid.* **95**, 136602 (2005).

[12] R. S. K. Mong and V. Shivamoggi, Phys. Rev. B **83**, 125109 (2011); A. M. Essin and V. Gurarie, *ibid.* **84**, 125132 (2011).

[13] H. C. Li, L. Sheng, and D. Y. Xing, Phys. Rev. Lett. **108**, 196806 (2012).

[14] E. Prodan, Phys. Rev. B **80**, 125327 (2009); New J. Phys. **12**, 065003 (2010).

[15] A. M. Essin and J. E. Moore, Phys. Rev. B **76**, 165307 (2007).

[16] T. Fukui and Y. Hatsugai, Phys. Rev. B **75**, 121403(R) (2007); T. Fukui, Y. Hatsugai, and H. Suzuki, J. Phys. Soc. Jpn. **74**, 1674-1677 (2005).

[17] H. C. Li, L. Sheng, D. N. Sheng, and D. Y. Xing, Phys. Rev. B **82**, 165104 (2010).

[18] W. Y. Shan, H. Z. Lu, and S. Q. Shen, New J. Phys. **12**, 043048 (2010).

[19] Z. Qiao, S. A. Yang, W. Feng, W.-K. Tse, J. Ding, Y. Yao, J. Wang, and Q. Niu, Phys. Rev. B **82**, 161414(R) (2010).

[20] Y. Yang, Z. Xu, L. Sheng, B. Wang, D. Y. Xing, and D. N. Sheng, Phys. Rev. Lett. **107**, 066602 (2011).

[21] C.-X. Liu, X. L. Qi, X. Dai, Z. Fang, and S.-C. Zhang, Phys. Rev. Lett. **101**, 146802 (2008).

[22] H. Li, L. Sheng, R. Shen, L. B. Shao, B. Wang, D. N. Sheng, and D. Y. Xing, Phys. Rev. Lett. **110**, 266802 (2013).

[23] W. Luo, D. X. Shao, M.-X. Deng, W. Y. Deng, and L. Sheng, Sci. Rep. **7**, 43049 (2017).

[24] S. K. Kim, H. Ochoa, R. Zarzuela, and Y. Tserkovnyak, Phys. Rev. Lett. **117**, 227201 (2016).

[25] M. Laubach, J. Reuther, R. Thomale, and S. Rachel, Phys. Rev. B **90**, 165136 (2014).

[26] J. Gregor, M. Messer, R. Desbuquois, M. Lebrat, T. Uehlinger, D. Greif, and T. Esslinger, Nature (London) **515**, 237 (2014).

[27] M. König, S. Wiedmann, C. Brüne, A. Roth, H. Buhmann, L. W. Molenkamp, X.-L. Qi, and S.-C. Zhang, Science **318**, 766 (2007).

[28] The spin gap is calculated from the spin projected Hamiltonian $H_{ij}(\boldsymbol{k}) = \langle\psi_i(\boldsymbol{k})|\sigma_0\tau_3|\psi_i(\boldsymbol{k})\rangle$ where $|\psi_i(\boldsymbol{k})\rangle$ denote the valence band wave functions $i = 1, 2$.

[29] The spin Chern number can be equivalently computed [20] using the two-dimensional effective projected spin operator $\mathcal{S}_{ij}(\boldsymbol{k}) = \langle V_i(\boldsymbol{k})|\sigma_0 \otimes \tau_3|V_j(\boldsymbol{k})\rangle$ with $i, j = 1, 2$ and $|V_{1,2}(\boldsymbol{k})\rangle$ represent the two valence band eigenvectors of Hamiltonian (2). After diagonalizing $\mathcal{S}(\boldsymbol{k})$ one obtains $|\psi_\pm(\boldsymbol{k})\rangle$ as eigenvectors corresponding to eigenvalues $\epsilon_\pm(\boldsymbol{k})$. Notice that $\epsilon_+(\boldsymbol{k}) = -\epsilon_-(\boldsymbol{k}) \neq 0$. One can employ Fukui's method to compute the spin Chern number $C_\uparrow$ and $C_\downarrow$ from $|\psi_+(\boldsymbol{k})\rangle$ and $|\psi_-(\boldsymbol{k})\rangle$, respectively. It is possible to construct the eigenvectors of the four-dimensional projected spin matrix $\tilde{S}$: $|\psi_1(\boldsymbol{k})\rangle = \langle\tau_3^+|\psi_+(\boldsymbol{k})\rangle|V_1(\boldsymbol{k})\rangle + \langle\tau_3^-|\psi_+(\boldsymbol{k})\rangle|V_2(\boldsymbol{k})\rangle$ and $|\psi_4(\boldsymbol{k})\rangle = \langle\tau_3^+|\psi_-(\boldsymbol{k})\rangle|V_1(\boldsymbol{k})\rangle + \langle\tau_3^-|\psi_-(\boldsymbol{k})\rangle|V_2(\boldsymbol{k})\rangle$. Here $|\tau_3^\pm\rangle$ represent the eigenstates of τ_3 with eigenvalues ±1. Similarly, from $|\psi_1(\boldsymbol{k})\rangle$ and $|\psi_4(\boldsymbol{k})\rangle$, one obtains spin Chern number $C_\uparrow$ and $C_\downarrow$ following the Fukui's method [16]. Both of the above definitions of projected spin operator are relied on the fact that both of them have two isolated islands, symmetrically placed around zero, in their eigenspectrum. The spectral projectors of the projected spin operator $\tilde{S}$ are $P_{\tilde{S}}(-, \boldsymbol{k})$ and $P_{\tilde{S}}(+, \boldsymbol{k})$, respectively, onto the negative and positive eigenvalues and they are smooth functions of $\boldsymbol{k}$. Therefore, $P_{\tilde{S}}(\boldsymbol{k})$ can be decomposed as follows: $P_{\tilde{S}}(\boldsymbol{k}) = P_{\tilde{S}}(-, \boldsymbol{k}) \oplus P_{\tilde{S}}(+, \boldsymbol{k})$ [14].

[30] Using the low energy expansion around the Dirac points($\alpha = \pm$), we obtain the following gap equations from four eigenenergies: $\delta E_1^\alpha = -\alpha M + \eta_{1,-} - \Delta_1$, $\delta E_2^\alpha = -\alpha M + \eta_{1,-} + \Delta_1$, $\delta E_3^\alpha = 2\Delta_1$, $\delta E_4^\alpha = -2\alpha M + \eta_{0,-}$, $\delta E_5^\alpha = -\alpha M + \eta_{-1,-} + \Delta_1$, $\delta E_6^\alpha = -\alpha M + \eta_{-1,-} - \Delta_1$ with $\eta_{a,\pm} = \sqrt{3}aV_{\rm so}\cos\phi + \frac{1}{2}(V_{\rm so} \pm 6\sqrt{3}t_2)\sin\phi$, $\Delta_1 = (M^2 + 3V_R^2 + (27t_2^2 + 3\sqrt{3}t_2V_{\rm so} + \frac{V_{\rm so}^2}{4})\sin^2\phi - 2\alpha M\eta_{0,+})$.

[31] T. Nag, V. Juricic, and B. Roy, Phys. Rev. Research **1**, 032045(R) (2019); Phys. Rev. B **103**, 115308 (2021); A. K. Ghosh, T. Nag, and A. Saha, *ibid.* **103**, 045424 (2021); **103**, 085413 (2021).

[32] B. A. Bernevig, T. L. Hughes, and S.-C. Zhang, Science **314**, 1757 (2006).

[33] A. Ström, H. Johannesson, and P. Recher, Phys. Rev. B **91**, 245406 (2015).

[34] M. Offidani and A. Ferreira, Phys. Rev. Lett. **121**, 126802 (2018).

[35] C. P. Orth, T. Sekera, C. Bruder, and T. L. Schmidt, Sci. Rep. **6**, 24007 (2016).

[36] N. Goldman and J. Dalibard, Phys. Rev. X **4**, 031027 (2014).

[37] J. Struck, J. Simonet, and K. Sengstock, Phys. Rev. A **90**, 031601(R) (2014).

[38] P. Wang, Z. Q. Yu, Z. Fu, J. Miao, L. Huang, S. Chai, H. Zhai, and J. Zhang, Phys. Rev. Lett. **109**, 095301 (2012).

[39] X. Zhou, X.-W. Luo, G. Chen, S. Jia, and C. Zhang, Phys. Rev. A **100**, 063630 (2019).

[40] B.-Z. Wang, Y.-H. Lu, W. Sun, S. Chen, Y. Deng, and X.-J. Liu, Phys. Rev. A **97**, 011605(R) (2018).

[41] Y.-J. Lin, K. Jimenez-Garcia, and I. B. Spielman, Nature (London) **471**, 83 (2011).

[42] L. Huang, Zengming Meng, Pengjun Wang, Peng Peng, S.-L. Zhang, L. Chen, D. Li, Q. Zhou, and J. Zhang, Nat. Phys. **12**, 540 (2016).

[43] Z. Meng, L. Huang, P. Peng, D. Li, L. Chen, Y. Xu, C. Zhang, P. Wang, and J. Zhang, Phys. Rev. Lett. **117**, 235304 (2016).

[44] W. Sun, B.-Z. Wang, X.T. Xu, C.R. Yi, L. Zhang, Z. Wu, Y. Deng, X.-J. Liu, S. Chen, and J.-W. Pan, Phys. Rev. Lett. **121**, 150401 (2018).

[45] R. Yu, W. Zhang, H.-J. Zhang, S.-C. Zhang, X. Dai, and Z. Fang, Science **329**, 61-64 (2010).

[46] D. Xiao, W. Zhu, Y. Ran, N. Nagaosa, and S. Okamoto, Nat. Commun. **2**, 596 (2011).

[47] A. M. Cook and A. Paramekanti, Phys. Rev. Lett. **113**, 077203 (2014).

[48] H. Zhang, C. Lazo, S. Blügel, S. Heinze, and Y. Mokrousov, Phys. Rev. Lett. **108**, 056802 (2012).
[49] H.-S. Kim and H.-Y. Kee, npj Quantum Mater. **2**, 20 (2017).
[50] Z. Qiao, W. Ren, H. Chen, L. Bellaiche, Z. Zhang, A. H. MacDonald, and Q. Niu, Phys. Rev. Lett. **112**, 116404 (2014).
[51] R.-A. Chang and C.-R. Chang, New J. Phys. **21**, 103019 (2019).
[52] R. Cardias, A. Bergman, A. Szilva, Y. O. Kvashnin, J. Fransson, A. B. Klautau, O. Eriksson, and L. Nordström, arXiv:2003.04680.
[53] S. Muhlbauer, B. Binz, F. Jonietz, C. Pfleiderer, A. Rosch, A. Neubauer, R. Georgii, and P. Böni, Science **323**, 915 (2009).
[54] T. Kurumaji, T. Nakajima, M. Hirschberger, A. Kikkawa, Y. Yamasaki, H. Sagayama, H. Nakao, Y. Taguchi, T.-H. Arima, and Y. Tokura, Science **365**, 914 (2019).
[55] W.-Y. Choi, H.-W. Bang, S.-H. Chun, S. Lee and M.-H. Jung, Nanoscale Res. Lett. **16**, 7 (2021).
[56] D. A. Gilbert, B. B. Maranville, A. L. Balk, B. J. Kirby, P. Fischer, D. T. Pierce, J. Unguris, J. A. Borchers, and K. Liu, Nat. Commun. **6**, 8462 (2015).
[57] K. F. Garrity and D. Vanderbilt, Phys. Rev. Lett. **110**, 116802 (2013).
[58] Y.-P. Huang, J.-W. Dong, P. Kotetes, and S. Zhou, Phys. Rev. B **102**, 195120 (2020).
[59] B. S. Kandemir, J. Phys. Soc. Jpn. **82**, 094706 (2013).
[60] L. Brey, Phys. Rev. B **92**, 235444 (2015).
[61] T. Frank. S. Irmer, M. Gmitra, D. Kochan, and J. Fabian, Phys. Rev. B **95**, 035402 (2017).
[62] A. Avsar, H. Ochoa, F. Guinea, B. Özyilmaz, B. J. van Wees, and I. J. Vera-Marun, Rev. Mod. Phys. **92**, 021003 (2020).
[63] D. Pesin and A. H. MacDonald, Nat. Mater. **11**, 409 (2012).
[64] R. Jansen, J. Phys. D **36**, R289 (2003).